Chemical Science

ROYAL SOCIETY OF CHEMISTRY

EDGE ARTICLE

View Article Online
View Journal

Cite this: DOI: 10.1039/d5sc09188h

All publication charges for this article have been paid for by the Royal Society of Chemistry

Structural and mechanistic basis of sulfolytic C–S bond cleavage by an Fe(II)/α-ketoglutarate-dependent sulfoquinovose dioxygenase

Mihwa Lee, * Ho N. N. Ho, Megan J. Maher, Guy N. L. Jameson * and Spencer J. Williams *

Received 24th November 2025
Accepted 8th February 2026

DOI: 10.1039/d5sc09188h

rsc.li/chemical-science

Sulfoquinovose dioxygenase (SqoD) enables bacterial carbon assimilation from the abundant sulfosugar sulfoquinovose (SQ) by Fe(II)/α-ketoglutarate (αKG)-dependent C–S bond cleavage. Here we report crystal structures of the *Marinobacterium aestuarii* enzyme (*Ma*SqoD) in multiple states with inert Mn^{2+} in place of Fe^{2+} (SQ-bound; Mn^{2+}·αKG; Mn^{2+}·αKG·SQ; Mn^{2+}·succinate), together with steady-state and pre-steady-state kinetics that link the structures with kinetically-inferred intermediates. The X-ray crystal structures show a canonical 2-His-1-carboxylate core metal center with SQ recognition *via* a mainly neutral network (Gln120, Trp253, backbone carbonyl of Ala185, and backbone amides of Ala89/Met118). Substrate binding triggers a hexacoordinate octahedral-to-pentacoordinate change at the metal center, unveiling a vacant site for O_2 in the fully assembled Mn^{2+}·αKG·SQ complex and thereby curbing uncoupled reactions. Pre-steady-state stopped-flow data support the canonical Fe(IV)=O chemistry of the dioxygenase and reveal an additional intermediate consistent with an enzyme-bound α-hydroxysulfonate or 6-dehydroglucose species. Together, these findings define the structural and mechanistic basis of sulfolytic SQ catabolism and illuminate the functional repertoire of Fe(II)/αKG-dependent dioxygenases in organosulfur carbon assimilation.

Introduction

Sulfoquinovose (SQ; 6-deoxy-6-sulfoglucose) is a ubiquitous sulfosugar that forms the polar headgroup of the sulfolipid sulfoquinovosyl diacylglycerol (SQDG), an essential component of photosynthetic membranes in plants, algae, and cyanobacteria (Fig. 1).[1] Billions of tonnes of SQDG are produced annually,[2,3] positioning this molecule as a central intermediate in the global sulfur cycle. Following delipidation of SQDG, the resulting glycoside sulfoquinovosyl glycerol (SQGro) is hydrolysed by dedicated sulfoquinovosidases from glycoside hydrolase families GH31 [4] or GH188,[5] releasing free SQ for bacterial catabolism.

Bacteria metabolize SQ through two distinct strategies: sulfoglycolysis and sulfolysis.[6,7] Sulfoglycolytic pathways cleave the carbon backbone of SQ to generate fragments that feed central metabolism, releasing smaller organosulfonates such as 2,3-dihydroxypropanesulfonate, sulfolactate, isethionate or sulfoacetate, which are further degraded by syntrophic partners.[8–14] In contrast, sulfolytic pathways directly cleave the carbon–sulfur bond of SQ, enabling complete oxidation of the carbon skeleton while liberating sulfur as sulfite or sulfate.

Two distinct sulfolytic mechanisms have been described. The first involves a flavin mononucleotide (FMN)-dependent monooxygenase system, in which SQ is oxidized to 6-dehydroglucose and sulfite, with a partner NADPH-dependent flavin reductase regenerating reduced FMN.[11,15] The second, more recently discovered, is the SQ dioxygenase (SqoD) pathway, identified in marine bacteria of the family Oceanospirillaceae such as *Marinomonas ushuaiensis* and *Marinobacterium aestuarii*,[16] and subsequently found in gammaproteobacteria, including family Alteromonadaceae such as *Alteromonas macleodii*.[3] In this system, an Fe^{2+}-dependent SQ:α-ketoglutarate (αKG) dioxygenase catalyzes oxidative C–S bond cleavage of SQ, producing 6-dehydroglucose and succinate (Fig. 1). Subsequent reduction of 6-dehydroglucose yields glucose for glycolysis, while oxidation of αKG to succinate couples SQ catabolism to the tricarboxylic acid cycle for cofactor regeneration. Members of the Oceanospirillaceae that possess this pathway uniformly encode GH188 sulfoquinovosidases for SQ liberation, while those of Alteromonadaceae use GH31 sulfoquinovosidases.

Fe(II)/αKG-dependent dioxygenases constitute one of the most functionally diverse families of non-heme iron enzymes, catalyzing hydroxylation, halogenation, desaturation, ring formation, and epimerization reactions, in both primary and secondary metabolism.[17,18] These enzymes are referred to as dioxygenases as both atoms of oxygen are incorporated into the

School of Chemistry, Bio21 Molecular Science and Biotechnology Institute, University of Melbourne, Parkville, Victoria 3010, Australia. E-mail: mihwa.lee@unimelb.edu.au; guy.jameson@unimelb.edu.au; sjwill@unimelb.edu.au

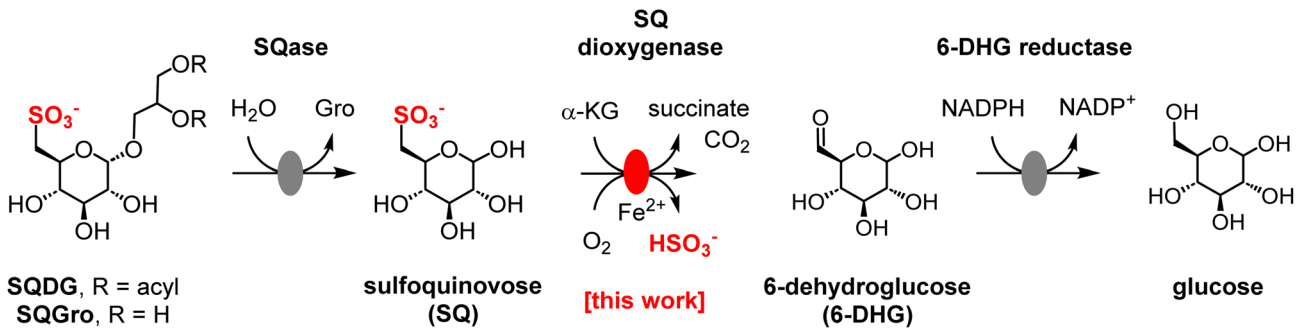

Fig. 1 Sulfolytic sulfoquinovose dioxygenase (sulfo-SDO) pathway in Oceanospirillaceae and Alteromonadaceae bacteria.

substrates, with one atom assimilated into succinate, and the other into the hydroxylated substrate. They share a conserved 2-His-1-carboxylate facial triad that coordinates the metal center and employ αKG as a co-substrate to activate molecular oxygen, generating a high-valent Fe(IV)=O intermediate that performs substrate oxidation.[19] While most members act on small-molecule or biosynthetic intermediates, the SQ dioxygenase (SqoD) represents a rare example of this superfamily operating in carbon assimilation and sulfur recycling.

Here, we describe the structure and mechanism of the Fe(II)/αKG-dependent SqoD from *M. aestuarii* (*Ma*SqoD), the namesake enzyme of the sulfo-SDO pathway. Crystal structures of *Ma*SqoD in complex with metal ions, the substrates αKG and SQ, and the product succinate, together with steady-state and single-turnover kinetic analyses, reveal the molecular basis of SQ recognition, oxygen activation, and C–S bond cleavage. These results define the chemical logic of sulfolytic SQ catabolism and expand the mechanistic scope of Fe(II)/αKG-dependent dioxygenases.

Results

Steady-state kinetic analysis of *Ma*SqoD

To gain deeper insight into the key enzyme of the sulfo-SDO pathway, we expressed recombinant SQ:α-ketoglutarate dioxygenase from *Marinobacterium aestuarii* (*Ma*SqoD). *Ma*SqoD enzyme activity was assessed by detecting one of the reaction products, sulfite, using a discontinuous assay in which sulfite production was quantified through a colorimetric reaction with Fuchsin-formaldehyde reagent. *Ma*SqoD exhibited optimal activity at pH 7.5 (Fig. S1), which was subsequently used for all further analyses. The addition of 0.25 mM Fe^{2+} in the presence of sodium L-ascorbate (0.5 mM) was required for enzyme activity, as purified *Ma*SqoD lacked detectable activity. None of the other divalent metals examined (Co^{2+}, Ni^{2+}, Mn^{2+}, and Zn^{2+}) supported activity. These findings confirm a previous report that *Ma*SqoD is an Fe(II)-dependent enzyme.[16]

The apparent Michaelis–Menten parameters of *Ma*SqoD were measured for SQ and αKG under apparent steady-state conditions, where the concentration of one substrate was held constant while the other was varied (Fig. 2 and Table 1). At 5 mM αKG, the pseudo-first-order parameters for SQ were $k_{cat}^{app} = 0.48 \pm 0.01\ s^{-1}$, $K_M^{app} = 1.7 \pm 0.2$ mM and $(k_{cat}/K_M)^{app} = (2.8 \pm 0.4) \times 10^2\ M^{-1}\ s^{-1}$, comparable to those reported previously ($k_{cat} = 0.16 \pm 0.01\ s^{-1}$, $K_M = 1.0 \pm 0.2$ mM, $k_{cat}/K_m = (1.6 \pm 0.3) \times 10^2\ M^{-1}\ s^{-1}$, at constant [αKG] = 5 mM).[16] When SQ was held constant at 5 mM and αKG was varied (0.05–15 mM), substrate inhibition was observed at higher αKG concentrations (Fig. 2b). Fitting the data to a substrate inhibition model yielded the following parameters for αKG: $k_{cat}^{app} = 0.73 \pm 0.01\ s^{-1}$, $K_M^{app} =$

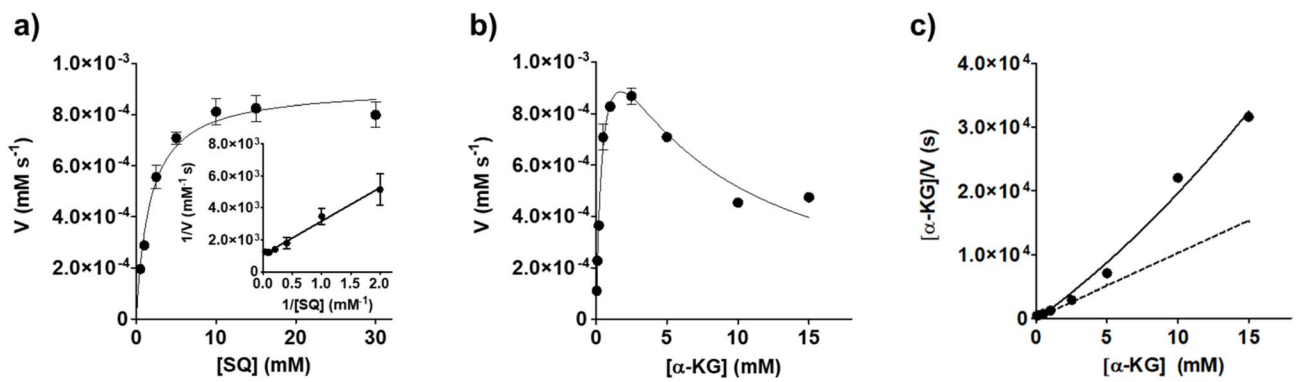

Fig. 2 *Ma*SqoD kinetic analysis. (a) Michaelis–Menten and Lineweaver–Burk double reciprocal plot for *Ma*SqoD activity with variable concentrations of SQ (0.5–30 mM) under apparent steady-state conditions with [αKG] fixed at 5 mM. (b) Substrate inhibition plot for *Ma*SqoD with varying αKG concentrations (0.05–15 mM) under apparent steady-state conditions with [SQ] fixed at 5 mM. (c) Hanes–Woolf plot of data from (b). Dotted line shows theoretical Michaelis–Menten relationship.

Table 1 Kinetic analysis of assorted substrates for SQ dioxygenase from *Marinobacterium aestuarii* (*Ma*SqoD)

Variable substrate	Constant substrate (concentration)	k_{cat}^{app} (s^{-1})	K_M^{app} (mM)	K_I^{app} (mM)	$(k_{cat}/K_M)^{app}$ (M^{-1} s^{-1})
SQ	αKG (5 mM)	0.48 ± 0.01	1.7 ± 0.2	—	280 ± 40
αKG	SQ (5 mM)	0.73 ± 0.07	0.5 ± 0.07	6.0 ± 0.9	1500 ± 300

0.5 ± 0.07 mM, K_I^{app} = 6.0 ± 0.9 mM and $(k_{cat}/K_M)^{app}$ = (1.5 ± 0.3) × 10^3 M^{-1} s^{-1}. While the k_{cat} value is consistent with that previously reported, the K_M and k_{cat}/K_M values differ by approximately 10-fold (k_{cat} = 0.73 ± 0.03 s^{-1}, K_M = 26 ± 4 μM, k_{cat}/K_M = (2.8 ± 0.4) × 10^4 M^{-1} s^{-1}, at constant [SQ] = 5 mM).[16] The reason for this inconsistency is not known. Moreover, no substrate inhibition was observed previously, although a lower maximum αKG concentration of 200 μM was used in the reported study. No measurable activity was observed when C_2/C_3-sulfonates (taurine, homotaurine, *R*- and *S*-dihydroxypropanesulfonate (DHPS), and *R*/*S*-cysteinolic acid) were used as substrate, confirming that *Ma*SqoD is an SQ-specific dioxygenase.

αKG inhibition of Fe(II)/αKG-dependent dioxygenases is unusual but not unprecedented. Millimolar inhibition by αKG was observed for AlkB DNA demethylase,[20] HIF prolyl hydroxylase,[21] factor inhibiting HIF,[22] and Jumonji C domain-containing histone demethylase.[23] We propose that inhibition arises from the binding of a second molecule of αKG within the SQ binding site, and competes with SQ binding. This hypothesis is indirectly supported by the observation that malonate, a structural analogue of αKG, binds in the SQ-binding site in the crystal structure described below.

Stopped-flow kinetic analysis of *Ma*SqoD reveals

Single turnover kinetics were investigated using stopped-flow spectroscopy, under conditions similar to those pioneered by Bollinger, Krebs *et al.* when studying *E. coli* taurine dioxygenase (*Ec*TauD).[24] The Fe(II)-loaded *Ma*SqoD:αKG:SQ complex, produced anaerobically in a glovebox, absorbed weakly in the visible region with a shoulder at 356 nm (745 M^{-1} cm^{-1}) and a maximum absorbance at 511 nm (450 M^{-1} cm^{-1}). This absorbance at 511 nm is slightly blue shifted from the comparable complex in *Ec*TauD, which absorbs maximally at 520 nm. Addition of anaerobic buffer did not change the spectrum showing the stopped flow was anerobic and the complex stable in our conditions.

Mixing the *Ma*SqoD : αKG : SQ complex 1 : 1 with oxygenated buffer at 4.5 °C in the stopped flow apparatus showed very subtle changes in the spectra recorded by the photo-diode array detector over the initial 4 s. These changes can be observed more easily by subtracting the final spectrum and presenting the data as difference spectra and by following single wavelength absorbance/time curves, as presented in Fig. 3. Over longer time periods (6–100 s), there are further changes, which were greater when using the photo-diode array than when the reaction was followed at a single wavelength. This appears to be

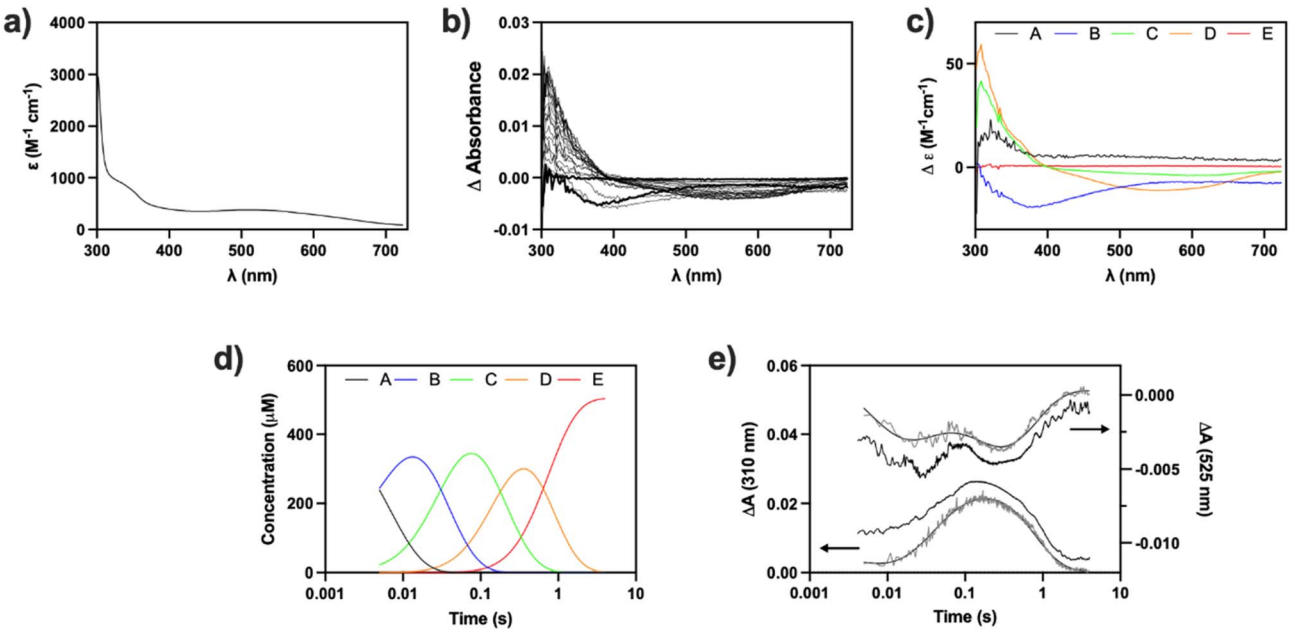

Fig. 3 Pre-steady state kinetic analysis of the *Ma*SqoD·Fe^{2+}·αKG·SQ complex mixed with oxygenated buffer at 4.5 °C. (a) Absorption spectrum of the anaerobically prepared *Ma*SqoD·Fe^{2+}·αKG·SQ complex. (b) Difference spectra obtained by subtracting the 4 s spectrum from earlier time points. (c) Component spectra and (d) corresponding concentration–time profiles derived from global fitting of the data to a linear reaction scheme (A → B → C → D → E). (e) Kinetic traces at 310 nm and 525 nm with fitted curves overlaid. Comparable single-wavelength traces recorded using a monochromator and photomultiplier detector are shown above and below for reference.

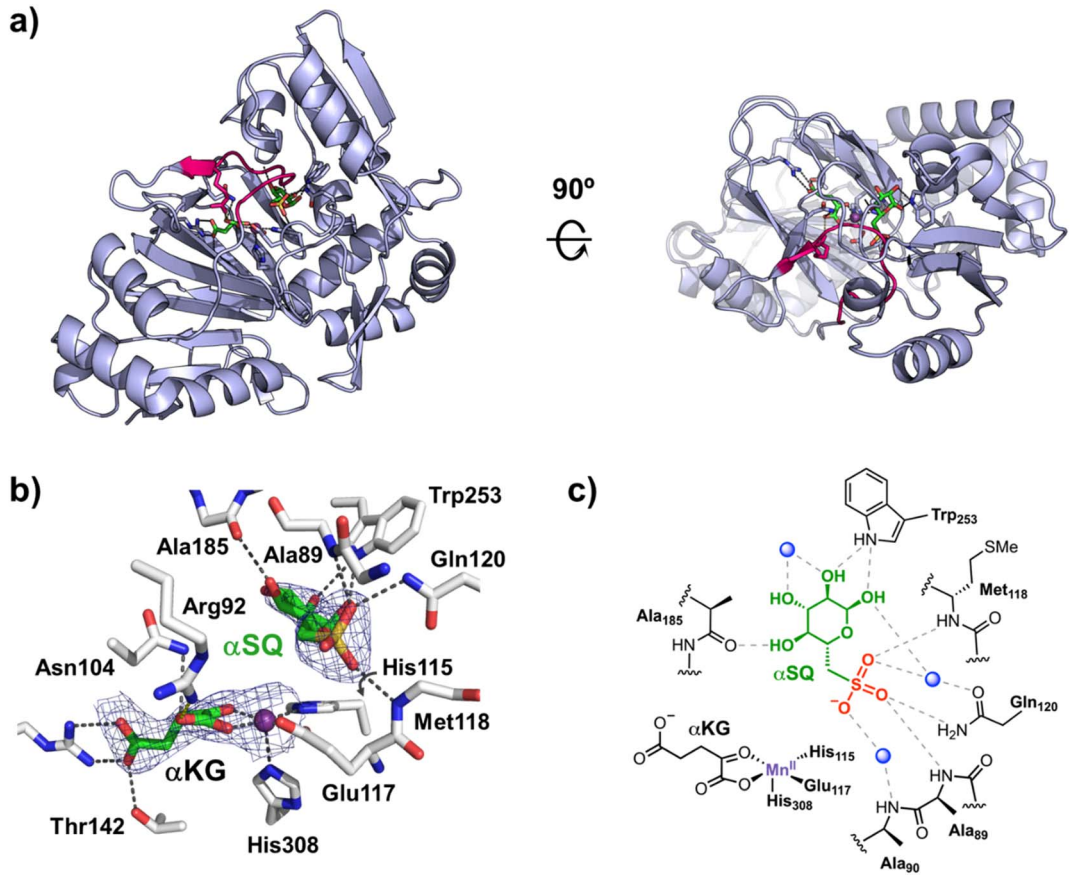

Fig. 4 Crystal structure of *Ma*SqoD·Mn^{2+}·αKG·SQ complex. (a) The overall structure of *Ma*SqoD in complex with Mn^{2+}, αKG, and SQ, is shown with the active-site flexible loop (residues 84–93) highlighted in magenta and the ligands bound in the active site shown in stick representation (b) Active site architecture in the *Ma*SqoD·Mn^{2+}·αKG·SQ complex. Electron density maps shown in blue mesh are $2F_o - F_c$ maps contoured at 1 σ. (c) A schematic illustration of key interactions in the SQ-binding mode in the complex. Blue spheres represent water molecules and dotted lines hydrogen bonds.

due to photo-reduction of the complex (most likely an iron(III) species) and thus is greater when the light intensity is higher when using white light and diode array detection (Fig. S2).

The absorbance-time data were fitted to a simple linear system of first order reactions. Initial fits used the model for TauD with three rate constants. The rate constants $k_1 = 150 \pm 3$ s^{-1}, $k_2 = 20.5 \pm 0.1$ s^{-1} and $k_3 = 0.99 \pm 0.01$ s^{-1} are comparable to *Ec*TauD (150 ± 2 s^{-1}, 12 ± 2 s^{-1}, 2.5 ± 0.5 s^{-1}). By comparison to *Ec*TauD, the first-rate constant refers to O_2 binding, the second to H-atom abstraction of SQ, and the third the release of the product(s). However, singular value decomposition of the data supported five species (A → B → C → D → E) (Fig. S3), providing a model-independent estimate of the number of kinetically-relevant species. Closer inspection of absorbance at 525 nm indicates that there is a third intermediate visible and this is ignored by the four-state model (A → D). Therefore, the

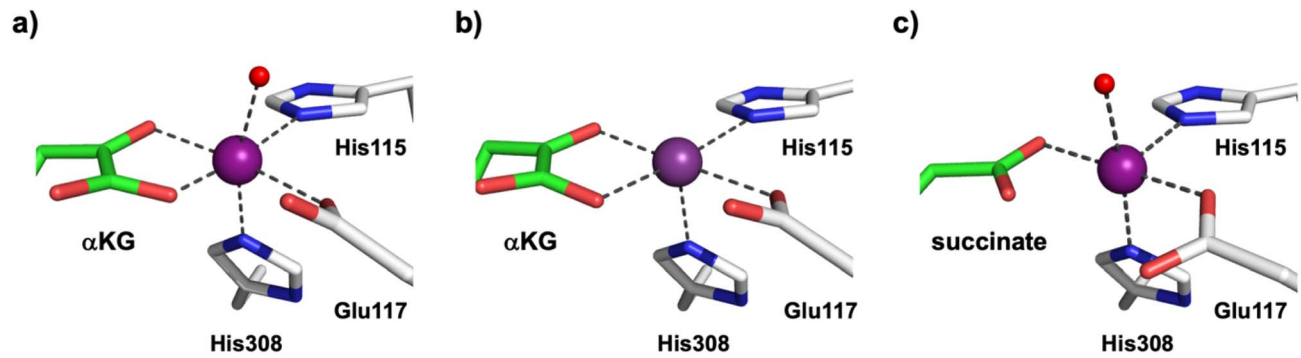

Fig. 5 Metal coordination geometry in *Ma*SqoD complexes. The zoomed-in metal centres in the crystal structures of (a) *Ma*SqoD·Mn^{2+}·αKG, (b) *Ma*SqoD·Mn^{2+}·αKG·SQ, and (c) *Ma*SqoD·Mn^{2+}·succinate complexes. Mn^{2+} is shown as purple spheres.

original kinetic data were fitted with four rate constants and five species, as shown in Fig. 3. The rate constants are $k_1 = 150 \pm 3$ s^{-1}, $k_2 = 30.6 \pm 0.3$ s^{-1}, $k_3 = 6.3 \pm 0.1$ s^{-1} and $k_4 = 1.8 \pm 0.3$ s^{-1}. This analysis proposes a new intermediate (D) with rate constants of formation and decay of k_3 and k_4, respectively. Since this intermediate appears after what we assign to H-atom abstraction according to the four-state model, we believe this shows either hydroxyl rebound or bisulfite release. Confirmation of the identity of this intermediate will require future work, which will be complicated by its low abundance that will make trapping difficult.

Structure of *Ma*SqoD·Mn^{2+}·αKG·SQ provides insight into the preassembled complex prior to oxygen activation

To define the structural basis of SQ oxidation, we obtained crystals of the *Ma*SqoD·Mn^{2+}·αKG·SQ complex by ligand exchange from *Ma*SqoD·$(malonate)_2$ crystals, which were grown under high concentration of sodium malonate (Fig. S4 and Table S1). In the malonate-bound structure, two malonate molecules occupy the αKG- and SQ-binding sites. Subsequent ammonium sulfate soaking and sequential incubation with Mn^{2+}, αKG, and SQ yielded the *Ma*SqoD·Mn^{2+}·αKG·SQ complex. Mn^{2+} was used as a chemically-inert surrogate for Fe^{2+} that preserves native coordination geometry. The resulting ternary complex structure refined to 2.10 Å resolution with partial metal and ligand occupancies (0.8) and represents a mimic of the catalytically competent state immediately prior to O_2 activation (Fig. 4). A Foldseek search identified a putative Fe(II)/αKG-dependent enzyme from *Arabidopsis thaliana* (At3g21360)[25] as the closest structural homologue (38.6% sequence identity, *E*-value of 1.2×10^{-41}), with much weaker similarity to *Ec*TauD (15.5% sequence identity, *E*-value of 8.9×10^{-12}) and other dioxygenases.

The ternary complex reveals a compact double-stranded β-helix ("jelly-roll") architecture characteristic of Fe(II)/αKG-dependent dioxygenases (Fig. 4a, S4 and Table S1). Two opposing β-sheets form a seven-stranded barrel that houses the catalytic centre. At the base of this barrel, the conserved 2-His-1-carboxylate facial triad (His115, Glu117, His308) coordinates the divalent metal. αKG binds in its canonical bidentate fashion *via* its keto and proximal carboxylate groups, while SQ occupies a pocket directly above the metal centre, positioning its C6 atom 4.2 Å from Mn^{2+}, the geometry expected for subsequent hydrogen abstraction and hydroxylation (Fig. 4b). This is comparable to the Fe^{2+}-C2 distance observed in the *Ec*TauD-Fe(II)·αKG·taurine complex (4.1 and 4.2 Å in chains A and B, respectively; PDB entry 1GY9).[26]

SQ is recognised through a predominantly neutral hydrogen-bond network formed by the side chains of Gln120, Trp253, the backbone amides of Ala89 and Met118, and the backbone carbonyl of Ala185. The sugar ring of SQ is coordinated by Trp253 and the carbonyl of Ala185; the Nε1 atom of Trp253 hydrogen-bonds to SQ C1-OH and C2-OH while the carbonyl of Ala185 to SQ C4-OH. The side chain of Gln120 and the backbone amides of Ala89 and Met118 form hydrogen bonds with the sulfonate group of SQ. Therefore, *Ma*SqoD contrasts with other organosulfonate-binding enzymes, which typically use positively charged residues such as Arg or Lys to engage the anionic sulfonate[5,27,28] (*e.g.*, Arg270 and His70 in *Ec*TauD[26]). A schematic of the complete interaction network is provided in Fig. 4c.

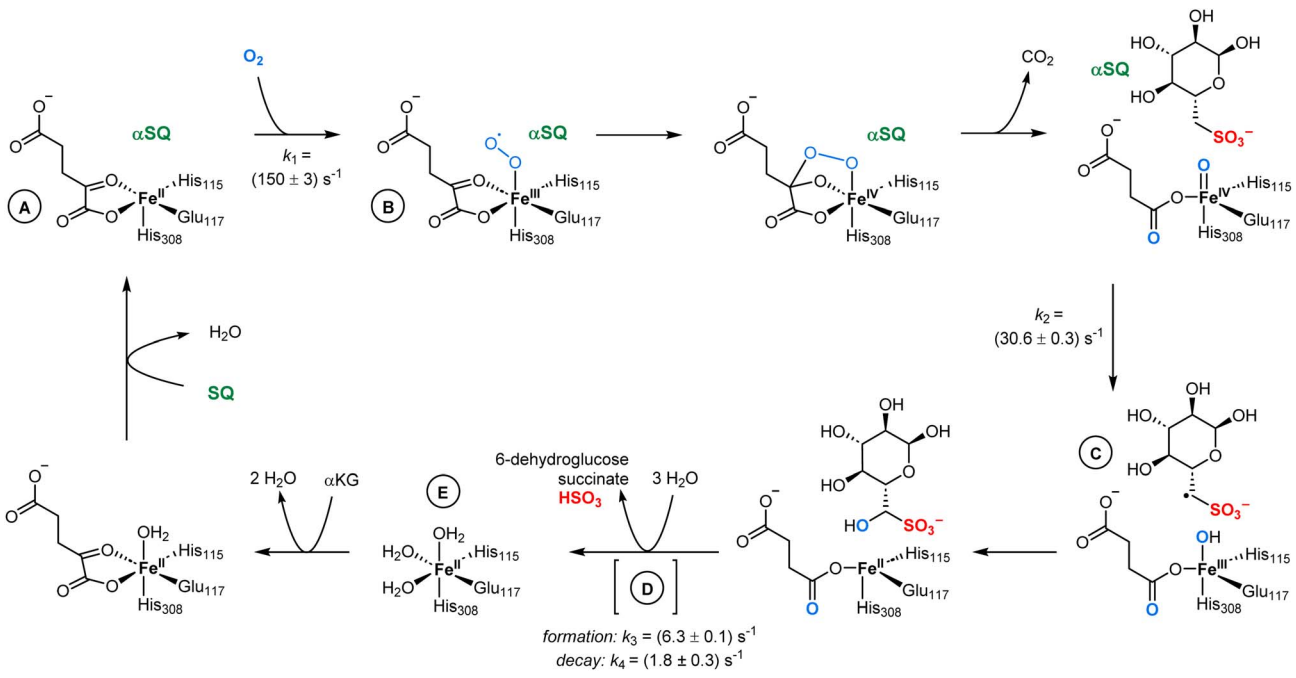

Fig. 6 Proposed catalytic mechanism of *Ma*SqoD showing the putative intermediates and associated rate constants determined in this work. The principal complexes (A–C, and E) correspond to species analogous to those characterized for *Ec*TauD. The nature of intermediate (D) remains uncertain and may represent an enzyme-bound α-hydroxysulfonate, 6-dehydroglucose, or sulfite species.

A loop spanning residues 84–93 sits directly above the active site and is well-ordered in this structure. Flexible active-site loops of this kind are a common structural element in Fe(II)/αKG-dependent dioxygenases and may shape or shield the catalytic pocket.[29,30] The backbone amides of Ala89 and Ala90 project toward the sulfonate-binding region, suggesting a role in gating access to the catalytic centre and coupling ligand binding to changes in metal coordination geometry. Because SQ, αKG, and Mn^{2+} are refined at partial occupancy (0.8) and the overall resolution of the ternary complex (2.10 Å) limits ligand detail, we also solved an SQ-only complex structure at 1.45 Å (Fig. S5). SQ binds with an almost identical orientation in the two complexes, confirming the placement and hydrogen-bonding interactions inferred from the full complex (Fig. S5d).

Metal and ligand complexes reveal the architecture of species along the reaction coordinate

To visualise complexes representing different stages of the catalytic cycle, crystals (sodium malonate exchanged with ammonium sulfate first) were soaked with Mn^{2+} and appropriate ligands to generate the *Ma*SqoD·Mn^{2+}·αKG and *Ma*SqoD·Mn^{2+}·succinate complexes (Fig. S6 and Table S1). The αKG-bound complex structure, refined to 2.04 Å and containing Mn^{2+} and αKG at partial occupancies (0.8), shows the metal centre in a distorted octahedral geometry ($\Delta = 0.0095$; $\sigma = 70.9°$). Here, Δ is the bond-length distortion index, defined as the average deviation of the six metal–ligand bond lengths from their mean value, and σ is the angular distortion parameter, defined as the root-mean-square deviation of the 12 *cis*-octahedral angles from the ideal 90°. These values are comparable to those of the alkylsulfatase AtsK from *Pseudomonas putida* ($\Delta = 0.0030$, $\sigma = 51.3°$).[31] In this structure, Mn^{2+} coordinates the facial triad, αKG, and a water ligand, with the water–Mn^{2+}–His308 angle (167°) showing a marked deviation from ideality (Fig. 5a). This hexacoordinate geometry represents the O_2-inactive precursor state prior to substrate binding. In the absence of the substrate SQ, a sulfate ion occupies the equivalent position of the SQ sulfonate and is recognised by Gln120 and the backbone amides of Ala89 and Met118.

The *Ma*SqoD·Mn^{2+}·αKG·SQ complex described above mimics the pentacoordinate, O_2-ready state of the catalytic ferrous complex. SQ binding displaces the water ligand and triggers an octahedral → square-pyramidal transition at the metal centre (Fig. 5b). The positions of αKG and the facial triad remain nearly identical to the αKG-only structure. These features collectively define the geometry required for O_2 activation.

The succinate-bound complex structure refined to 1.57 Å displays a pentacoordinate Mn^{2+} (facial triad, one succinate oxygen, and water) (Fig. 5c). Relative to the αKG-bound state, Glu117Oε2 shifts below the coordination plane (hydrogen-bonding to Tyr85) (Fig. S6), and the water–Mn^{2+}–His308 angle (174°) differs from that in the αKG-bound state (167°). These subtle rearrangements propagate outward so that the 84–93 loop adopts a more open conformation (Ala90 Cα–Ala90 Cα distance increases by 0.92 Å); Arg92 switches from coordination of αKG to coordination of a sulfate ion (mimicking sulfite); and the adjacent 181–190 and 253–263 loops move outward (Fig. S7). This more open conformation likely facilitates dissociation of succinate and the transient α-hydroxysulfonate/6-dehydroglucose intermediate, consistent with the slow kinetic phase observed in stopped-flow experiments ($k_4 = 1.8 \pm 0.3\ s^{-1}$).

Discussion

SQ dioxygenases catalyze the oxidative cleavage of sulfonate groups from the sulfosugar SQ, thereby releasing carbon that would otherwise be metabolically inaccessible due to the chemical inertness of the C–S bond. In *Marinomonas ushuaiensis*, the SqoD product 6-dehydroglucose is reduced to glucose for glycolysis while sulfite is released. In contrast, most Fe(II)/αKG-dependent dioxygenases acting on sulfonates support sulfur acquisition rather than carbon assimilation. The prototype is TauD from *Escherichia coli*, which cleaves taurine to produce sulfite for sulfur assimilation.[32] Other examples include a yeast homologue more active on taurocholate and isethionate,[33] and the sulfatases AtsK from *Pseudomonas putida*[31] and Rv3406 from *Mycobacterium tuberculosis*[34] that cleave alkyl sulfate monoesters to sulfate. These cases illustrate how the Fe(II)/αKG scaffold has diversified toward either sulfur acquisition or, in the case of SqoD, for sulfolytic carbon assimilation. Our kinetic analysis identified inhibition of *Ma*SqoD by αKG at high, millimolar concentrations. While the significance of this observation is unclear, it has been noted that in *E. coli* under conditions of nitrogen starvation intracellular levels of αKG rise to 10 mM or more.[35] Possibly, inhibition of SqoD under conditions of elevated αKG could serve to limit flux through the SQ assimilation pathway to prevent metabolic overflow.

The single-turnover kinetics of *Ma*SqoD align with the canonical Fe(II)/αKG-dependent dioxygenase mechanism (Fig. 6). Molecular oxygen binds to the iron center and rapidly reacts with αKG, forming a highly reactive Fe(IV)-oxo species. This step is energetically favorable due to the concomitant decarboxylation of αKG to succinate and CO_2 ($\Delta_r G° = -275$ kJ mol^{-1} for αKG → succinate + CO_2).[36] The Fe(IV)-oxo intermediate then abstracts a hydrogen atom from SQ, generating a ferric-hydroxide and an SQ radical. Subsequent hydroxyl rebound[37] yields the initial product: SQ hydroxylated at the C6 position. In the case of *Ec*TauD, it is unclear whether elimination of the α-hydroxysulfonate to give sulfite and aminoacetaldehyde occurs in the active site of the enzyme or upon release from the enzyme. In our case we find kinetic evidence for a new intermediate that may reflect bound α-hydroxysulfonate or 6-dehydroglucose, suggesting that elimination of α-hydroxysulfonate to give sulfite and 6-dehydroglucose occurs in the active site of the enzyme. In the organophosphonate taurine analogue, 2-aminoethylphosphonate, two enzymes are required for the comparable C–P bond cleavage. α-hydroxylation catalysed by Fe(II)/αKG-dependent PhnY yields a stable α-hydroxyphosphonate[38] that requires a second oxidative step catalyzed by PhnZ to cleave C–P.[39]

*Ma*SqoD adopts the canonical double β-sheet "jelly-roll" architecture characteristic of Fe(II)/αKG-dependent dioxygenases and includes the conserved 2-His-1-carboxylate facial triad (His115, Glu117, His308), which coordinates the divalent metal center. A series of chemically-inert Mn^{2+} complexes provide insight into the αKG-, αKG·SQ-, and succinate-bound complexes. Binding of SQ triggers a transition from octahedral to penta-coordinate metal geometry, revealing an open coordination site for O_2 only when both SQ and αKG are present, an arrangement that minimizes uncoupled turnover. While built upon a common jelly-roll architecture, members of this enzyme family exhibit variations in the flexible loop and in the domain positioned above the substrate-binding pocket, adaptations that enable recognition of diverse primary and secondary metabolites. In *Ma*SqoD, SQ recognition is achieved through a neutral hydrogen-bonding network involving (Gln120 and Trp253), the backbone carbonyl of Ala185, and the backbone amides of Ala89 and Meta118. The backbone amides (Ala89 and Met118) and Gln120 coordinate the sulfonate oxygens in place of the cationic Arg/Lys clamps seen in *Ec*TauD. This neutral binding environment, combined with a perpendicular orientation of Trp253 to the sugar ring and flanking hydrophobic residues Ile186 and Val249, creates a substrate-binding pocket that is distinct from that of *Ec*TauD (Fig. S8). Upon conversion of αKG to succinate, Arg92 shifts from coordinating the co-substrate to engaging a sulfate ion (which may mimic the α-hydroxysulfonate or released sulfite), while the flexible loop spanning residues 84–93 adopts a more open conformation, possibly facilitating product release and re-entry of αKG. Collectively, these observations suggest that *Ma*SqoD achieves substrate selectivity and catalysis through coupling of metal coordination geometry, loop dynamics, and a neutral sulfonate-binding motif that together orchestrate oxygen activation only in the fully assembled ternary complex.

Conclusions

SQ dioxygenases illustrate how Fe(II)/αKG-dependent enzymes couple specialized catabolic reactions to central carbon metabolism: αKG acts as the electron sink, is oxidatively decarboxylated to succinate, and is subsequently replenished through downstream metabolic processes (*e.g.*, β-oxidation products or 6-dehydroglucose → glycolysis → tricarboxylic acid cycle), preserving flux balance. Similar αKG regenerative loops operate in Fe(II)/αKG-dependent dioxygenase utilizing pathways in phenoxyalkanoate herbicide degradation,[40] and aerobic lysine degradation *via* L-2-hydroxyglutarate.[41,42]

*Ma*SqoD repurposes the Fe(II)/αKG-dependent dioxygenase scaffold for sulfosugar catabolism, unlocking carbon from SQ. Structures of SQ-, αKG-, αKG·SQ-, and succinate-bound states reveal the canonical 2-His-1-carboxylate motif and a substrate-triggered hexacoordinate octahedral → penta-coordinate trigonal pyramidal switch, which gates O_2 activation in the ternary complex. SQ specificity is conferred by a largely neutral recognition network (Gln120, backbone amides and a backbone carbonyl) framed by a perpendicular Trp253. Pre-steady-state kinetics support Fe(IV)=O formation and identify a transient species consistent with an enzyme-bound α-hydroxysulfonate/6-dehydroglucose intermediate, implicating on-enzyme sulfite elimination. Together, these results define the structural logic of sulfolytic C–S scission and show how Fe(II)/αKG enzymology is integrated into carbon assimilation.

Author contributions

S. J. W. conceived the project. M. L. performed protein production and crystallography. H. N. performed Michaelis–Menten enzyme kinetics, G. N. L. J. performed single turnover kinetics. M. J. M. provided expert advice on crystallisation and interpretation of inorganic geometry in crystal structures. M. L., G. N. L. J., and S. J. W. designed experiments, analyzed data and wrote the manuscript.

Conflicts of interest

The authors declare no competing interests.

Data availability

Structural data (atomic coordinates) have been deposited with the Protein Data Bank (PDB accession codes: 9YUT (malonate-bound *Ma*SqoD), 9YUU (*Ma*SqoD·SQ), 9YUV (*Ma*SqoD·Mn^{2+}·αKG), 9YUW (*Ma*SqoD·Mn^{2+}·αKG·SQ), and 9YUX (*Ma*SqoD·Mn^{2+}·succinate)).[43a–e]

Supplementary information (SI): Fig. S1–S8, Table S1, experimental details, supplementary references (PDF). See DOI: https://doi.org/10.1039/d5sc09188h.

Acknowledgements

This work was supported by the Australian Research Council (DP250100819, DP230102668, DP240100126), M. L. is a recipient of Kaye Merlin Brutton Bequest Funding (University of Melbourne). Aspects of this research were undertaken on the Macromolecular Crystallography beamlines at the Australian Synchrotron (Victoria, Australia), part of ANSTO, and made use of the Australian Cancer Research Foundation (ACRF) detector. We thank the Australian Synchrotron beamline staff for their professional support.

References

1 E. D. Goddard-Borger and S. J. Williams, *Biochem. J.*, 2017, **474**, 827–849.
2 A. B. Roy, A. J. Ellis, G. F. White and J. L. Harwood, *Biochem. Soc. Trans.*, 2000, **28**, 781–783.
3 X. Ma, H. Wang, C. Dong, L. Liu, X. Qiu, X. Chen, Q. Chen, L. Wang, Y. Zhang, N. Jiao, S. J. Williams and K. Tang, *Nat. Commun.*, 2025, **17**, 209.
4 G. Speciale, Y. Jin, G. J. Davies, S. J. Williams and E. D. Goddard-Borger, *Nat. Chem. Biol.*, 2016, **12**, 215–217.
5 A. Kaur, I. B. Pickles, M. Sharma, N. Madeido Soler, N. E. Scott, S. J. Pidot, E. D. Goddard-Borger, G. J. Davies and S. J. Williams, *J. Am. Chem. Soc.*, 2023, **145**, 28216–28223.

6 A. J. D. Snow, L. Burchill, M. Sharma, G. J. Davies and S. J. Williams, *Chem. Soc. Rev.*, 2021, **50**, 13628–13645.
7 Y. Wei, Y. Tong and Y. Zhang, *Biosci. Rep.*, 2022, **42**, BSR20220314.
8 B. Frommeyer, A. W. Fiedler, S. R. Oehler, B. T. Hanson, A. Loy, P. Franchini, D. Spiteller and D. Schleheck, *iScience*, 2020, **23**, 101510.
9 K. Denger, M. Weiss, A. K. Felux, A. Schneider, C. Mayer, D. Spiteller, T. Huhn, A. M. Cook and D. Schleheck, *Nature*, 2014, **507**, 114–117.
10 A. K. Felux, D. Spiteller, J. Klebensberger and D. Schleheck, *Proc. Natl. Acad. Sci. U. S. A.*, 2015, **112**, E4298–E4305.
11 J. Liu, Y. Wei, K. Ma, J. An, X. Liu, Y. Liu, E. L. Ang, H. Zhao and Y. Zhang, *ACS Catal.*, 2021, **11**, 14740–14750.
12 J. Mayer, T. Huhn, M. Habeck, K. Denger, K. Hollemeyer and A. M. Cook, *Microbiology*, 2010, **156**, 1556–1564.
13 Y. Wei and Y. Zhang, *Annu. Rev. Biochem.*, 2021, **90**, 817–846.
14 J. Ruff, K. Denger and A. M. Cook, *Biochem. J.*, 2003, **369**, 275–285.
15 M. Sharma, J. P. Lingford, M. Petricevic, A. J. D. Snow, Y. Zhang, M. A. Järvå, J. W.-Y. Mui, N. E. Scott, E. C. Saunders, R. Mao, R. Epa, B. M. da Silva, D. E. V. Pires, D. B. Ascher, M. J. McConville, G. J. Davies, S. J. Williams and E. D. Goddard-Borger, *Proc. Natl. Acad. Sci. U. S. A.*, 2022, **119**, e2116022119.
16 Z. Ye, Y. Wei, L. Jiang and Y. Zhang, *iScience*, 2023, **26**, 107803.
17 S. Zhao, L. Wu, Y. Xu and Y. Nie, *Nat. Prod. Rep.*, 2024, **42**, 67–92.
18 R. P. Hausinger, *Crit. Rev. Biochem. Mol. Biol.*, 2004, **39**, 21–68.
19 K. D. Koehntop, J. P. Emerson and L. Que Jr., *J. Biol. Inorg. Chem.*, 2005, **10**, 87–93.
20 R. W. Welford, I. Schlemminger, L. A. McNeill, K. S. Hewitson and C. J. Schofield, *J. Biol. Chem.*, 2003, **278**, 10157–10161.
21 S. Pektas, C. Y. Taabazuing and M. J. Knapp, *Biochemistry*, 2015, **54**, 2851–2857.
22 V. D. Chaplin, M. A. Valliere, J. A. Hangasky and M. J. Knapp, *J. Inorg. Biochem.*, 2018, **178**, 63–69.
23 B. Cascella and L. M. Mirica, *Biochemistry*, 2012, **51**, 8699–8701.
24 J. C. Price, E. W. Barr, B. Tirupati, J. M. Bollinger and C. Krebs, *Biochemistry*, 2003, **42**, 7497–7508.
25 E. Bitto, C. A. Bingman, S. T. M. Allard, G. E. Wesenberg, D. J. Aceti, R. L. Wrobel, R. O. Frederick, H. Sreenath, F. C. Vojtik, W. B. Jeon, C. S. Newman, J. Primm, M. R. Sussman, B. G. Fox, J. L. Markley and G. N. Phillips Jr., *Acta Crystallogr., Sect. F*, 2005, **61**, 469–472.
26 J. M. Elkins, M. J. Ryle, I. J. Clifton, J. C. Dunning Hotopp, J. S. Lloyd, N. I. Burzlaff, J. E. Baldwin, R. P. Hausinger and P. L. Roach, *Biochemistry*, 2002, **41**, 5185–5192.
27 M. Sharma, P. Abayakoon, R. Epa, Y. Jin, J. P. Lingford, T. Shimada, M. Nakano, J. W. Y. Mui, A. Ishihama, E. D. Goddard-Borger, G. J. Davies and S. J. Williams, *ACS Cent. Sci.*, 2021, **7**, 476–487.
28 M. Sharma, N. Pudlo, M. A. Järvå, A. Kaur, A. John, L. Burchill, J. P. Lingford, R. Epa, P. Abayakoon, N. E. Scott, J. P. Turkenburg, G. J. Davies, E. C. Martens, E. D. Goddard-Borger and S. J. Williams, *J. Biol. Chem.*, 2025, **301**, 108320.
29 S. H. Knauer, O. Hartl-Spiegelhauer, S. Schwarzinger, P. Hänzelmann and H. Dobbek, *FEBS J.*, 2012, **279**, 816–831.
30 A. Höppner, N. Widderich, M. Lenders, E. Bremer and S. H. J. Smits, *J. Biol. Chem.*, 2014, **289**, 29570–29583.
31 I. Müller, A. Kahnert, T. Pape, G. M. Sheldrick, W. Meyer-Klaucke, T. Dierks, M. Kertesz and I. Usón, *Biochemistry*, 2004, **43**, 3075–3088.
32 J. M. Bollinger Jr, J. C. Price, L. M. Hoffart, E. W. Barr and C. Krebs, *Eur. J. Inorg. Chem.*, 2005, 4245–4254.
33 D. A. Hogan, T. A. Auchtung and R. P. Hausinger, *J. Bacteriol.*, 1999, **181**, 5876–5879.
34 K. M. Sogi, Z. J. Gartner, M. A. Breidenbach, M. J. Appel, M. W. Schelle and C. R. Bertozzi, *PLoS One*, 2013, **8**, e65080.
35 F. Huergo Luciano and R. Dixon, *Microbiol. Mol. Biol. Rev.*, 2015, **79**, 419–435.
36 M. E. Beber, M. G. Gollub, D. Mozaffari, K. M. Shebek, A. I. Flamholz, R. Milo and E. Noor, *Nucleic Acids Res.*, 2022, **50**, D603–D609.
37 T. M. Pangia, C. G. Davies, J. R. Prendergast, J. B. Gordon, M. A. Siegler, G. N. L. Jameson and D. P. Goldberg, *J. Am. Chem. Soc.*, 2018, **140**, 4191–4194.
38 F. R. McSorley, P. B. Wyatt, A. Martinez, E. F. DeLong, B. Hove-Jensen and D. L. Zechel, *J. Am. Chem. Soc.*, 2012, **134**, 8364–8367.
39 L. M. van Staalduinen, F. R. McSorley, K. Schiessl, J. Séguin, P. B. Wyatt, F. Hammerschmidt, D. L. Zechel and Z. Jia, *Proc. Natl. Acad. Sci. U. S. A.*, 2014, **111**, 5171–5176.
40 R. H. Müller and W. Babel, *Appl. Environ. Microbiol.*, 2000, **66**, 339–344.
41 S. Knorr, M. Sinn, D. Galetskiy, R. M. Williams, C. Wang, N. Müller, O. Mayans, D. Schleheck and J. S. Hartig, *Nat. Commun.*, 2018, **9**, 5071.
42 M. Zhang, C. Gao, X. Guo, S. Guo, Z. Kang, D. Xiao, J. Yan, F. Tao, W. Zhang, W. Dong, P. Liu, C. Yang, C. Ma and P. Xu, *Nat. Commun.*, 2018, **9**, 2114.
43 (*a*) M. Lee, Crystal structure of malonate-bound sulfoquinovose dioxygenase from Marinobacterium aestuarii, 9YUT, 2026, DOI: 10.2210/pdb9YUT/pdb; (*b*) M. Lee, Crystal structure of sulfoquinovose dioxygenase from Marinobacterium aestuarii in complex with sulfoquinovose, 9YUU, 2026, DOI: 10.2210/pdb9YUU/pdb; (*c*) M. Lee, Crystal structure of sulfoquinovose dioxygenase from Marinobacterium aestuarii in complex with Mn(II) and alpha-ketoglutarate, 9YUV, 2026, DOI: 10.2210/pdb9YUV/pdb; (*d*) M. Lee, Crystal structure of sulfoquinovose dioxygenase from Marinobacterium aestuarii in complex with Mn(II), alpha-ketoglutarate, and sulfoquinovose, 9YUW, 2026, DOI: 10.2210/pdb9YUW/pdb; (*e*) M. Lee, Crystal structure of sulfoquinovose dioxygenase from Marinobacterium aestuarii in complex with Mn(II) and succinate, 9YUX, 2026, DOI: 10.2210/pdb9YUX/pdb.